Solar Phys (2009) 256: 111–130
DOI 10.1007/s11207-009-9346-5

Forward Modeling of Coronal Mass Ejections Using STEREO/SECCHI Data

A. Thernisien · A. Vourlidas · R.A. Howard

Received: 8 December 2008 / Accepted: 27 March 2009 / Published online: 10 April 2009

Abstract We describe a forward modeling method developed to study the coronal mass ejections observed with STEREO/SECCHI. We present a survey of 26 CMEs modeled with this method. We selected most of the bright events observed since November 2007 to August 2008, after when the separation was greater than 40° degrees, thus showing noticeable differences between the two views. From these stereoscopic observations and using a geometric model of a flux rope, we are able to determine the three-dimensional direction of propagation, the three-dimensional velocity and acceleration of the CME front, and in most of the cases the flux rope orientation and length. We define a merit function that allows us to partially automate the fit, as well as perform a sensitivity analysis on the model parameters. We find a precision on the longitude and latitude to be of a maximum of $\pm 17°$ and $\pm 4°$, respectively, for a 10% decrease of the merit function but a precision on the flux rope orientation and length to be almost one order of magnitude larger, showing that these parameters are more difficult to estimate using only coronagraph data. Finally, comparison with independent measurements shows a good agreement with the direction and speed we estimated.

Keywords Solar corona · CME · Forward modeling · Stereoscopy

STEREO Science Results at Solar Minimum
Guest Editors: Eric. R. Christian, Michael L. Kaiser, Therese A. Kucera, O.C. St. Cyr.

A. Thernisien (✉)
Universities of Space Research Association, 10211 Wincopin Circle, Suite 620, Columbia, MD 21044, USA
e-mail: arnaud.thernisien@nrl.navy.mil

A. Vourlidas · R.A. Howard
Naval Research Laboratory, Code 7663, 4555 Overlook Avenue SW, Washington, DC 20375, USA

A. Vourlidas
e-mail: angelos.vourlidas@nrl.navy.mil

R.A. Howard
e-mail: russell.howard@nrl.navy.mil

1. Introduction

The *Solar Terrestrial Relations Observatory* (STEREO) mission was successfully launched in October 2006. Its two twin spacecraft were injected into two orbits around the Sun, with perihelia slightly inside of Earth's orbit and slightly outside of Earth's orbit. This causes them to drift apart from Earth at a rate of approximately 22.5° per year in each direction, one leading Earth and one trailing. Aboard STEREO is the Sun Earth Connection Coronal and Heliospheric Investigation (SECCHI) instrument package (Howard *et al.*, 2008), comprising five different imaging telescopes, which together allow a view from the solar disk to 1 AU. One of the main goals of the STEREO mission is to better understand coronal mass ejections (CMEs).

We observe CMEs in white-light emission arising from Thomson scattering of photospheric light by the free electrons of the coronal plasma (Minnaert, 1930; Billings, 1966). Because the corona is optically thin in the visible, we only observe the projection of the three-dimensional (3D) CME structure integrated along the instrumental lines of sight. The main challenge is then to understand and determine the 3D morphology and kinematics of these phenomena using the STEREO multiviewpoint observations.

The problem of reconstructing the electron density of the solar corona from one, two, or even three viewpoints has no unique solution and is ill-posed: Assumptions and/or regularization have to be used to obtain a stable solution. The solution depends on what kind of assumptions can be made and what their limitations are. There are basically three categories of methods that can be used for the reconstruction of the solar corona: inverse methods, triangulation methods, and forward modeling.

Three different inverse methods have been used to reconstruct the solar corona: (1) solar rotational tomography (SRT), (2) combining interplanetary scintillation (IPS) measurements with coronagraph data, and (3) the Pixon method. In the first technique, Frazin and colleagues (Frazin and Janzen, 2002; Frazin and Kamalabadi, 2005a, 2005b) used a sequence of Large Angle and Spectrometric Coronagraph (LASCO) data collected during half a solar rotation and were able to reconstruct the corona during a quiet period using tomography. The method has been validated using a 3D MHD model of the corona (Vásquez *et al.*, 2008). This method requires 14 days of continuous observations during which it is assumed that the corona evolves slowly, making it unsuitable for CME reconstruction. Frazin *et al.* (2005) have shown that Kalman filtering could be used to take into account temporal variations and that it would be possible to apply this method with a shorter time sequence by combining STEREO-A and STEREO-B data. Jackson *et al.* (2006) combined IPS measurements with the Solar Mass Ejection Imager (SMEI) data (Eyles *et al.*, 2003) to reconstruct the 28 October 2003 CME. The SMEI instrument records the white-light Thomson scattering of the coronal density structures, while IPS measurements are used to constrain the location of the density along the lines of sight. Finally, the Pixon technique, primarily developed for image restoration (Puetter, Gosnell, and Yahil, 2005), has been used by Antunes, Thernisien, and Yahil (2009) to reconstruct the CME event of 31 December 2007 from the STEREO/SECCHI observations. They were able to determine the kinematics of the upper and lower components of this highly distorted flux-rope event. This technique makes use of synchronized views of the corona and is based on minimizing the number of electron density volumetric elements necessary to reproduce the observations.

The second category of reconstruction uses triangulation methods, also called stereogrammetry or tie-point methods. This technique is largely used to make topological maps of terrain or buildings. It consists in localizing, either by eye or automatically, the same feature

in at least two different views of the same scene. This is a strong assumption in the case of the optically thin corona. Nevertheless, Liewer *et al.* (2007, 2008, 2009), and Mierla *et al.* (2008) demonstrated that the technique can be used to determine CME 3D direction and speed, as well as to reconstruct filament eruptions. Note that this method only provides the location of a feature but not the electron density.

Finally, forward modeling techniques consist in making strong assumptions on the morphology of the feature that is intended to be reconstructed. Usually, an analytical function of the 3D electron density distribution is introduced that utilizes parameters for controlling the shape of the feature. Compared to an inverse reconstruction, where the density cube represents N^3 free parameters to be determined, forward modeling only requires a few parameters to sufficiently define a model. The problem consists then in estimating those parameters that will best fit the model to the observations. An important point of the technique is the choice of the model, which should be based on physical considerations if possible. Also, the number of free parameters should be sufficiently restrained so that a unique solution can be determined. It should be noted that the resultant solution is only unique with respect to the assumed model. This method was applied in the first estimations of the coronal electron density. The assumptions of local spherical symmetry of the electron density and of a decreasing density profile as a polynomial of the inverse of the radial distance, r, allowed Minnaert (1930), Van de Hulst (1950), and Saito, Poland, and Munro (1977) and more recently Quémerais and Lamy (2002) to estimate the electron density radial profile for the quiet Sun in coronal holes and streamers.

In the case of more complex and transient structures such as CMEs, Fisher and Munro (1984) used a so-called ice cream cone model to determine the electron density of a CME observed with the Mk III coronagraph. The cone model has been used to determine the geometrical and kinematical properties of halo CMEs observed with SOHO/LASCO (Zhao, Plunkett, and Liu, 2002; Xie, Ofman, and Lawrence, 2004), and more recently, Zhao (2008) has shown that the method could be extended to STEREO/SECCHI observations. Thernisien, Howard, and Vourlidas (2006) used an analytical model of a flux rope to fit 34 events observed with LASCO-C2. Because one view is not sufficient to determine the depth of the CME with respect to the plane of the sky, they used the position of the CME source region observed with the Extreme Ultraviolet Imaging (EIT) telescope (Cremades and Bothmer, 2004) to position their model in space. Now that we have stereoscopic observations from STEREO/SECCHI, this ambiguity can be removed and the unprojected 3D direction of a CME can be determined using only coronagraph data. For example, Pizzo and Biesecker (2004) presented a method in which they combined triangulation and geometrical modeling to determine the CME trajectories using STEREO/SECCHI observations. Boursier (2007) and Boursier, Lamy, and Llebaria (2009) also developed an automatic procedure intended to determine the position and trajectory of CMEs observed with STEREO/SECCHI by comparing a library of simulated images of geometric models with the observed images.

In the present study, we use the Graduated Cylindrical Shell (GCS) model of Thernisien, Howard, and Vourlidas (2006) to fit 26 CME events observed by the SECCHI/COR2 A and B instruments. We start with a short review on the flux-rope morphology of CMEs and on the GCS model itself and proceed to describe the details of the fitting method. We focus on fitting the geometric parameters of the model only and not the actual electron density of the leading edge as we did in Thernisien, Howard, and Vourlidas (2006). We also introduce a merit function to allow a sensitivity analysis of the model parameters for the different modeled events. Finally, we compare our results with other methods and present our conclusions.

2. The Flux-Rope CME Morphology

The observed shapes of the CMEs vary from event to event and are generally categorized based on their morphological similarities (Howard *et al.*, 1985). Over the years, a three-part morphology has attracted particular attention (Illing and Hundhausen, 1985). It can be seen as a bright front surrounding a dark cavity, which itself surrounds a bright core. The tremendous amount and quality of the data gathered by SOHO/LASCO (Brueckner *et al.*, 1995) has revealed much more details of these structures, especially circular striations around the cavity, showing that most of the CMEs could be seen as flux-rope or flux-tube-like structures. Models of idealized flux ropes have been also successful in reproducing the observations (Chen *et al.*, 1997) and analyses of their properties (Vourlidas *et al.*, 2000; Krall and St. Cyr, 2006) have shown that they are consistent with theoretical flux ropes and magnetically dominated systems. Further work has also shown that CMEs tend to expand in a self-similar manner (Chen, 1996; Chen *et al.*, 1997, 2000). More generally, the different theoretical models also tend to agree at least on the flux-rope morphology, even though initiation mechanisms, for example, could be different (see Forbes *et al.*, 2006, for a description of these different models). As a result, the concept of flux-rope morphology is now well accepted in the community.

3. The Graduated Cylindrical Shell or Hollow Croissant Model

The GCS is meant to reproduce the large-scale structure of flux-rope-like CMEs (Thernisien, Howard, and Vourlidas, 2006). It consists of a tubular section forming the main body of the structure attached to two cones that correspond to the "legs" of the CME. The resulting shape is reminiscent of a hollow croissant because electrons are placed only at the surface and the prominence material is not modeled. Figures 1(a) and (b) show, respectively, a face-on and an edge-on representation of the model. The dash-dotted line represents the axis of the model and the solid line the outline of the shell, where the density is placed. Here h is the height of the legs and α is the half-angle between the legs. The cross section of the model is a circular annulus of varying radius, a, given by

$$a(r) = \kappa r, \tag{1}$$

where r is the distance from the center of the Sun to a point at the edge of the shell and κ the aspect ratio of the loop.[1] This equation implies that the model can be easily adopted to treat the CME at different heights using self-similar expansion.

The apex, or the leading edge of the model noted h_{front}, can be calculated using the following formula:

$$h_{\text{front}} = h\,\frac{1}{1-\kappa}\,\frac{1+\sin\alpha}{\cos\alpha}. \tag{2}$$

The electron density is placed on the shell by using a Gaussian-like function, peaked at the distance $a(r)$ from the loop axis:

[1] The parameter κ can be compared to $1/\Lambda$ in Chen *et al.* (1997).

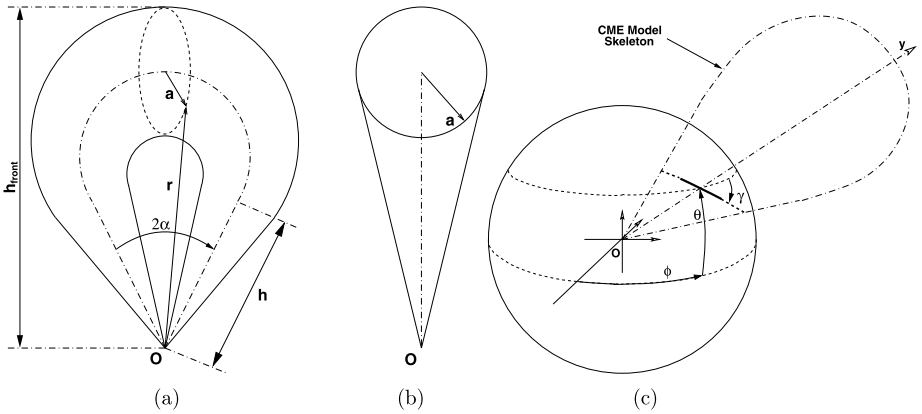

Figure 1 Representations of the Graduated Cylindrical Shell (GCS) model (a) face-on and (b) edge-on. The dash-dotted line is the axis through the center of the shell. The solid line represents a planar cut through the cylindrical shell and the origin. O corresponds to the center of the Sun. (c) Positioning parameters. The loop represents the axis through the center of the shell, ϕ and θ are the longitude and latitude, respectively, and γ is the tilt angle around the axis of symmetry of the model.

$$N_{\mathrm{e}}(d) = N_{\mathrm{e}} \exp\left[-\left(\frac{d-a}{\sigma_s}\right)^2\right],$$
$$\text{with } \sigma_s = \begin{cases} \sigma_{\text{trailing}} & \text{if } d < a, \\ \sigma_{\text{leading}} & \text{if } d \geq a. \end{cases} \tag{3}$$

Finally, the model can be positioned in space using spherical coordinates, as shown in Figure 1(c): ϕ and θ are the longitude and the latitude, respectively, and γ is the tilt angle around the axis of symmetry of the model.

Here, we focus only on the geometric aspect of the modeling, leaving the photometric aspect (*i.e.*, the electron density) to be addressed in future studies. Accordingly, we do not compare the observed total brightness images directly to the corresponding total brightness rendered model images, but rather we compare the overall observed shape to what we define to be the wireframe of the hollow croissant. The wireframe representation is simply the set of points located on the surface of the croissant, where the profile of electron density is peaked. The advantage of using a wireframe is that it allows real-time rendering, whereas it requires few seconds to few minutes for a full Thomson scattering rendering. Figure 2 shows two synthetic coronagraph images and two wireframe images of the model, viewed in the same orientation as in Figures 1(a) and (b), face-on and edge-on, respectively. The two top images are generated using a ray-tracing renderer that takes full account of the Thomson scattering equations; the two bottom images show only the projection of the wireframe on the virtual CCD. This demonstrates clearly that the wireframe representation reproduces accurately the geometry of the Thomson scattering view.

4. The Data

Although this technique can be applied to images from all the instruments of the SECCHI package, we focus our study mostly on the COR2 data since its field of view (FOV) is well adapted to observe fully developed flux-rope-like CMEs. Indeed, the flux rope might not be

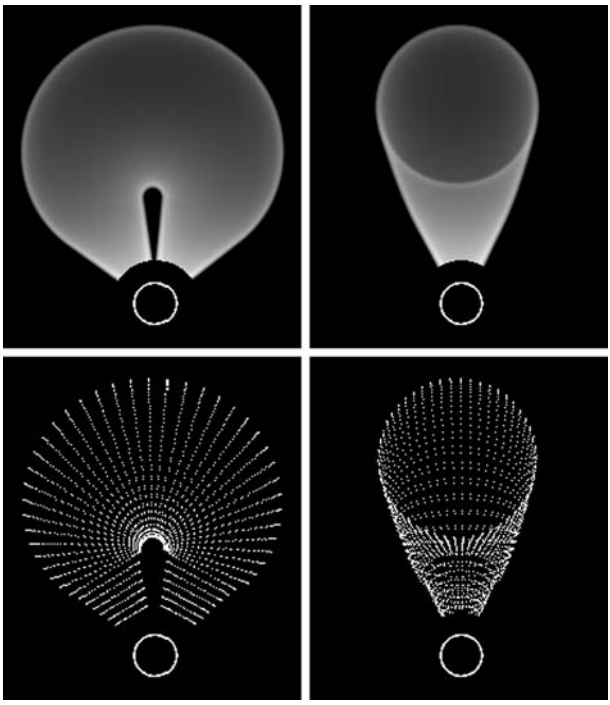

Figure 2 Comparison between white-light and wireframe rendering. On top are the simulated white-light images using Thomson scattering of the GCS model as seen in Figures 1(a) and (b). At the bottom are the corresponding wireframe views.

fully developed in the COR1 FOV, while its overall structure becomes too faint and more difficult to interpret in the Heliospheric Imagers' (HI) FOV. Nevertheless, we used COR1 data when the event could be clearly identified and followed in both COR1 views. We did not use the HI images because the flux rope appearance can be distorted by the effects of interactions with the solar wind.

The images are prepared using the standard SolarSoft `secchi_ prep.pro` procedure. We use calibrated total brightness images from that we subtract from a pre-event image (base difference).

5. Method

The method is based on the comparison between a synchronized stereoscopic pair of SECCHI images and the wireframe projection of the model. A graphic user interface (GUI) has been developed to allow interactive change of the model parameters and to display the projected wireframe overlaid on top of the pair of stereo images. The computation of the projected wireframe takes into account the spacecraft attitude at the time of the image acquisition and the projection type of the instrument (Calabretta and Greisen, 2002). The fit is initially done interactively until the wireframe projection matches both data views. An automatic optimizer can be used as a second step to refine the fit. This procedure is repeated for each stereo pair of the CME time sequence, so that the evolution of the parameters can be recorded.

The feature we intend to fit is the leading outer front of the CME. Once this feature is identified in the stereo image pair, we apply the following method to interactively fit the model using the GUI:

1. Start with a pair of COR2 images where the CME front is developed and visible in both views.
2. Start with the parameter α set to 0. Adjust the longitude, latitude, and height parameters until a good visual match is obtained. Adjust the aspect ratio to match the spatial extension of the CME.
3. Now adjust α and γ to refine the fit. All the other parameters might have to be slightly adjusted too.
4. Outline by hand the outer front of the CME and use an automatic optimizer to refine and finalize the fit.
5. Use the other images of the sequence and fit the model at the different times.
6. Fit the COR1 images when the feature can be clearly identified in both A and B.

For the first step, we choose a COR2 image pair where the CME front is well above $5R_{\odot}$. Because the front appears larger, this facilitates the visualization and therefore allows a better fit. We call this stereo pair the reference pair.

The goal of step 2 is to find a first estimate of the CME direction. Setting the parameter α to 0 makes the model similar to the so-called ice cream cone model (Fisher and Munro, 1984): The front of the model is no longer a tubular loop but now a hemispherical shell. We freeze this degree of freedom for the moment because it has a minor influence on finding the direction of the CME. Instead, we adjust the longitude, latitude, height, and (slightly) the aspect ratio, which is a parameter relative to the spatial extent of the CME.

Once the initial estimate of the CME position is obtained, step 3 consists of adjusting the last two parameters, α and γ, to improve the visual agreement. In the next section we discuss why, in some cases, the fit could not be improved even when using these two additional degrees of freedom.

Step 4 consists of using a user-defined contour of the CME outer front and running an automatic optimizer to refine the fit. We discuss this step in more detail in Section 6. Note that we only use this automatic fit step for the reference pair of images.

Finally, in steps 5 and 6, we perform the fit to the rest of the data sequence to obtain the time evolution of the parameters. In the majority of the events, we obtain a good agreement just by varying the height to follow the propagation of the CME front. In some cases, minor corrections may need to be applied to other parameters. In this study, we consider them fixed and leave this analysis for further study.

6. Goodness of Fit and Optimization

Because the fit is done interactively, the results depend on the user's expertise and interpretation of the phenomenon. We did not select any "well-behaved" events based, say, on the brightness or smoothness of the front as we did in Thernisien, Howard, and Vourlidas (2006). To the contrary, we chose events as varied as possible, without concerns about their shape complexity and/or brightness levels. For this reason, we describe in the following the criteria used to identify the CME outer front and to define a measure of how well the model was able to reproduce an observed shape. We also show how the fitting process can be automated and its limitations.

We define the CME outer front as the outermost bright front moving radially across the instrument FOV. Because the wireframe represents the points of the model where the density is peaked, the observable feature we intend to fit is then the peak of brightness of this front. In most of the bright events this feature can be clearly identified in the data images, but this identification can be more difficult in some cases, mostly because we do not observe

one single front and/or it is weak or "washed out" in the surrounding background. For the reader's benefit, in the summary of the results, we give the polar coordinates and the angular extent of the leading edge in the observed images.

Once the front is identified, we use our graphic interface to outline it by hand. We use this contour to evaluate a goodness of fit function: It is based on the comparison of this contour with the binary contour of the model wireframe projection. This is formalized as follows:

$$F(\mathbf{v}) = \frac{1}{n} \sum_{i=1}^{n} \sum_{j=1}^{N_i} c_{i,j} e_{i,j}(\mathbf{v}), \tag{4}$$

with $\mathbf{v}$ the vector of parameters of the model; i the index corresponding to the views (in our case, we have $n = 2$ views for STEREO-A and STEREO-B); N the number of points of the images, $c_{i,j}$ the pixel j of the user-defined contour for the view i; and finally, $e_{i,j}(\mathbf{v})$ the pixel j of the contour of the wireframe projection for the view i. $F(\mathbf{v})$ is maximum when all the pixels of $\mathbf{c}$ and $\mathbf{e}$ coincide on both views, giving this way a measure of the goodness of fit.

Fitting the model to the data consists then in maximizing $F(\mathbf{v})$:

$$\hat{\mathbf{v}} = \underset{\mathbf{v}}{\operatorname{argmax}}\, F(\mathbf{v}). \tag{5}$$

Because $\mathbf{c}$ and $\mathbf{e}$ are binary images, $F(\mathbf{v})$ can present sudden jumps and numerous local maxima, making this merit function unsuitable for an automatic optimization. To smooth $F(\mathbf{v})$, we actually use a filtered version of the user-defined contour (denoted $\mathbf{c}'$ hereafter):

$$\mathbf{c}' = \mathbf{c} * N_{2\mathrm{D}}\left(1, \sigma^2\right), \tag{6}$$

where $N_{2\mathrm{D}}(1, \sigma^2)$ is the 2D normal distribution function of mean 1 and variance σ^2, and $*$ is the 2D convolution operator. Typically, we found that using a σ of 7 pixels on 512×512 images was sufficient to smooth out most of the local minima.

To illustrate this, Figure 3 shows three cases of merit function. Figure 3(a) shows an unsmoothed merit function. We can see that it presents numerous local maxima. Since we use an optimizer that bases its search on the local gradient, the optimization will just get trapped in the first local maximum encountered. To deal with this problem, as we stated in the previous paragraph, we smooth the merit function. An example is shown on Figure 3(b). This has the effect of removing most of the local maxima but with the drawback that now the merit function is broader. As a consequence, this will slightly slow down the convergence speed of the optimizer and also decrease the precision.

We use a Powell (Press *et al.*, 2003) optimization routine to partially automatize the fit. The parameters are initialized close to the best solution to avoid the optimizer from taking too long and getting trapped in a local maximum. Moreover, only the longitude, latitude, and height are left variable while the other parameters are left fixed. Indeed, some parameters are still degenerate even with two points of view, so no unique solution can be found. We discuss this case in Section 7.

Finally, this merit function allows us to perform a sensitivity analysis of the model parameters. We performed this analysis for all the events and the results are discussed in Section 8.

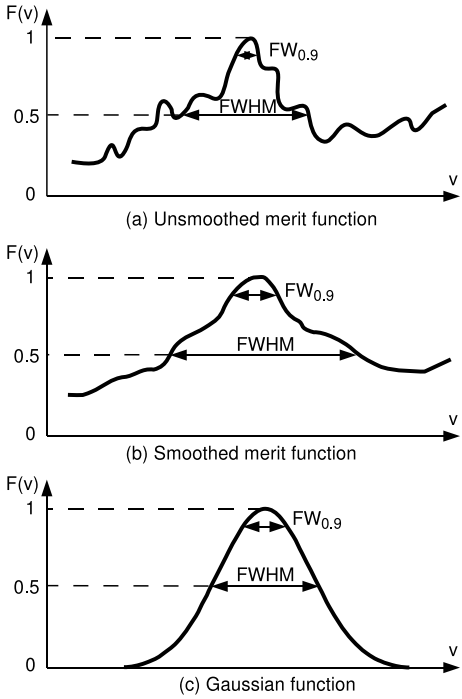

Figure 3 Illustration of three different merit functions. The first one, labeled (a), presents many local maxima. The second one, labeled (b), is a smoothed version of (a). This removes most of the local maxima but makes the function broader, which will affect the convergence speed of the optimizer. The third graph, (c), shows a Gaussian function. It is shown to compare the full width at half maximum (FWHM) of the three functions, as well as the full width for a 10% decrease ($FW_{0.9}$).

7. Examples

We present here three examples of event fitting. We chose the different cases to illustrate the technique and its limitations.

7.1. CME of 26 April 2008

The pair of COR2 images for this CME are shown in the first row of Figure 4. We see that the CME travels toward the east in the FOV of A, and it appears as a halo in the FOV of B. This example shows the difficulty in identifying the CME leading edge in both views: Two fronts seem to be present in both A and B images. The second row of Figure 4 shows the same A and B data images but with the contour, outlined by hand, of the leading edge we intend to fit with the GCS model. Finally, the last row of Figure 4 shows again the same two data images but this time with the wireframe of the GCS model overlaid. We see a good visual agreement between the model outer contour position and the CME front. The second front, appearing as a quasicircular halo in B, is more reminiscent of the pileup of material by the compression wave of the CME.

7.2. CME of 29 January 2008

The second example, presented in Figure 5, corresponds to the event of 29 January 2008. In both the B and the A views (first row of Figure 5), this event presents a circular, rim-shaped front, suggesting a flux rope seen edge-on, and with its plane of symmetry almost coplanar with the plane of the ecliptic. In this case, we see that it is not possible to determine accurately the length of the flux rope, which is controlled by the parameter α: This parameter

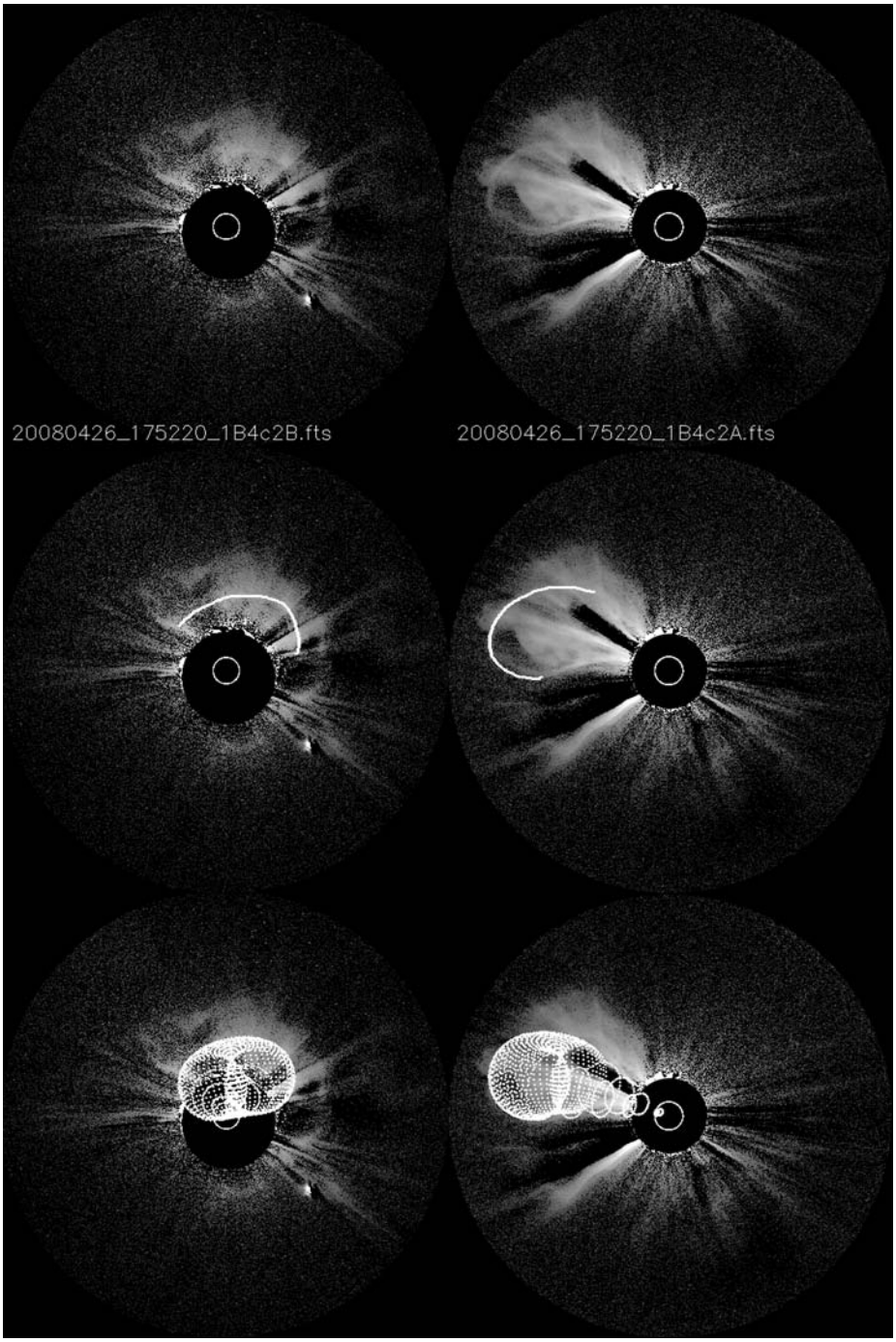

Figure 4 Modeling of the 26 April 2008 event. The first two images in the top row are the pair of COR2 B and A data images, taken at 17:52 UT. The second row shows the same images but with the contour, drawn by hand, of the leading edge we intend to fit. Finally, the last row shows again the same B and A data images, with this time the GCS wireframe overlaid on top.

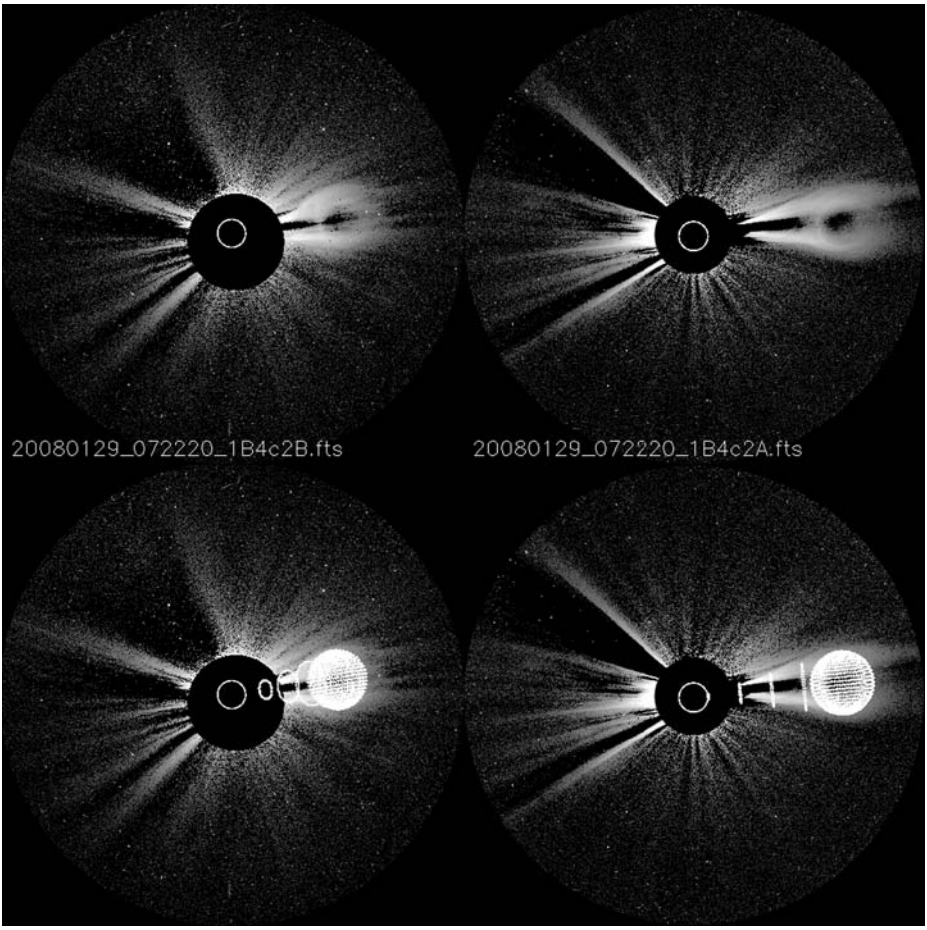

Figure 5 Example of model fit for the event of 29 January 2008 observed at 7:20 UT in COR2 B and A (top row). The second row shows the same images with the wireframe fit overlaid. It is not possible to determine accurately the flux-rope length in this case.

is said to be degenerate. A polar view, or at least a view from a few tens of degrees out of the ecliptic plane, would be necessary to remove that degeneracy in such a case.

7.3. CME of 31 December 2007

The last example, shown in Figure 6, is the CME of 31 December 2007. The front of this event appears to be strongly distorted. In this case, the GCS model does a poor job reproducing this type of front, even though it gives a good first estimate of the 3D direction and the spatial extension of the CME. We found in this particular case that the front can be divided into two lobes, located above and below the dip in the front. This is especially visible in A. We have then used two hemispherical shells (parameter α set to 0) to fit both the upper and lower lobes, allowing more accurate estimations of their spatial extensions and their trajectories. The wireframe representation of these two shells is shown in the second row of Figure 6.

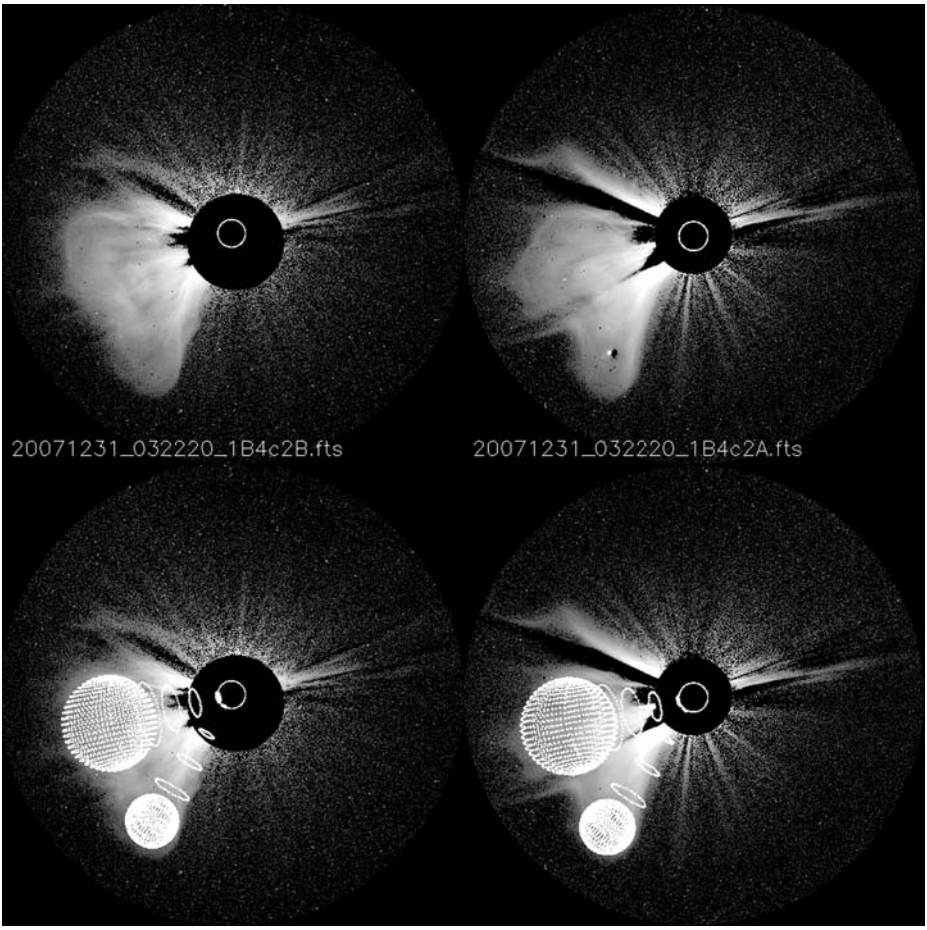

Figure 6 Example of model fit for the event of 31 December 2007 observed at 3:22 UT in COR2 B and A (top row). The front of the event is strongly distorted, especially viewed from A. We model the two observed lobes with two hemispherical shells (bottom row).

8. Results and Discussion

The results of the modeling for the 26 studied events are given in Table 1. One first remark is that there are three entries for the 31 December 2007 event. Since the front of this event is strongly distorted (see example in Section 7.3 and Figure 6), the first row corresponds to an average fit and the two other ones correspond to the upper lobe and the lower lobe, as shown in Figure 6.

The second remark concerns the tilt angle, γ, and the half angular width, α. There are three cases: (1) α can be measured, (2) α is degenerate, and (3) the CME front is distorted or weak. In case (1), the measured values are just entered in Table 1. Case (2) corresponds to a flux rope seen edge-on, which is illustrated and discussed in the example of Section 7.2. In that case, we enter 0 for the tilt angle and a question mark in the half-angle column since it is not possible to determine this parameter. Finally, case (3) is when the CME front is too distorted or too weak to allow a determination of the flux-rope orientation. In this case, we

Table 1 Summary of the results for the 26 modeled events. The first two columns give the date and the time of the COR2 stereo pair used as the reference. The next six columns give the position of the CME front in the data images. Columns PA1a and PA2a, as well as the columns PA1b and PA2b, give the polar angle boundaries of the front, measured respectively in A and B. Columns Ea and Eb are the maximum projected height of the front, measured as well in A and B. The next six columns give the value of the different parameters of the CGS model. The longitude and latitude, ϕ and θ, are given in the Stonyhurst coordinate system (Thompson, 2006): In this coordinate system, Earth is always at longitude 0. Finally, column F gives the value of the goodness of fit (see Equation (4)), and a comment column is used to provide additional qualitative information on the event and/or the modeling. EO stands for edge-on.

Event date	Time	PA1a	PA2a	PA1b	PA2b	Ea	Eb	h_f	ϕ	θ	γ	α	κ	F	Comments
	(UT)	(degrees)				($R_\odot$)			(degrees)				Ø	(%)	
04-Nov-2007	22:52	58	104	25	112	13.8	9.0	14.9	−44	12	10	9	0.31	78	
16-Nov-2007	15:52	242	284	227	290	12.2	8.1	12.4	123	−14	0	?	0.31	66	EO
04-Dec-2007	15:22	260	310	261	300	10.3	11.9	11.9	71	4	0	?	0.29	79	EO
16-Dec-2007	17:52	86	130	85	131	6.5	12.8	19.6	−151	−3	−47	10	0.28	74	Weak
31-Dec-2007	03:22	75	157	79	159	12.0	12.2	13.8	−80	−25	90	16	0.40	34	All
31-Dec-2007	03:22	75	124	79	124	11.4	11.3	12.4	−91	−5	–	0	0.35	73	Upper lobe
31-Dec-2007	03:22	124	157	124	159	12.0	12.2	12.7	−91	−48	–	0	0.17	78	Lower lobe
02-Jan-2008	13:22	71	129	69	151	13.4	8.0	14.1	−51	−9	–	0	0.42	66	Distorted
23-Jan-2008	06:22	132	238	89	167	10.7	12.6	15.9	−162	−28	−49	8	0.4	77	
29-Jan-2008	07:22	262	288	261	295	12.0	9.4	11.9	107	3	0	?	0.21	97	EO
04-Feb-2008	13:52	74	125	Halo		13.5	5.4	16.5	-21	−9	–	0	0.28	81	Weak in B
12-Feb-2008	15:22	225	267	213	265	11.5	11.4	12.4	93	−26	−14	9	0.29	78	
13-Feb-2008	19:52	32	89	308	20	10.4	6.0	13.9	−18	11	−7	8	0.26	80	Weak in B
15-Feb-2008	16:22	70	110	60	122	13.5	9.2	14	−60	−2	0	?	0.29	89	EO
24-Feb-2008	05:22	25	91	56	100	10.1	13.7	14.2	−122	20	2	11	0.27	77	
17-Mar-2008	17:52	264	340	266	296	5.5	10.5	11.1	40	4	2	6	0.20	93	Weak in A

Table 1 (*Continued.*)

Event date	Time	PA1a	PA2a	PA1b	PA2b	Ea	Eb	h_f	ϕ	θ	γ	α	κ	F	Comments
	(UT)	(degrees)				($R_\odot$)			(degrees)				Ø	(%)	
18-Mar-2008	13:22	102	138	119	129	9.3	9.4	10.3	−83	−31	13	25	0.09	90	
25-Mar-2008	20:52	68	124	75	132	12.1	11.5	12.4	−84	−12	−20	21	0.34	76	
05-Apr-2008	17:52	243	290	234	299	12.1	8.5	12.8	126	4	−7	16	0.31	78	Fit of inner front only
26-Apr-2008	17:52	40	93	279	11	12.4	6.5	15.1	−21	6	13	8.4	0.22	83	Multifront, halo in B
17-May-2008	12:22	69	122	31	180	12.4	7.8	12.9	−45	−13	9	7	0.35	79	Weak in B
24-May-2008	00:22	142	239	231	253	7.9	14.1	14.6	39	−23	2	18	0.10	89	
02-Jun-2008	08:52	58	117	Halo		13.8	7.2	14.5	−37	−3	2	8	0.35	80	Weak in B, part of the leading edge missing in A
12-Jun-2008	11:22	48	97	53	96	9.2	11.5	11.5	−92	9.5	−8	12	0.26	52	Distorted and weak
26-Jun-2008	07:22	339	60	55	104	3.9	10.2	11.6	−147	2	0	?	0.31	91	EO, weak in A
07-Jul-2008	20:22	89	147	102	253	12.6	6.7	14.5	−23	−18	1	16	0.28	78	Leading edge interrupted in A and B
31-Jul-2008	23:52	265	307	287	11	12.4	5.9	13.0	141	13	−1	7	0.30	78	Weak
07-Aug-2008	17:22	86	119	89	156	13.2	8.1	13.6	−54	−14	−1	3	0.27	80	Weak in B

Table 2 Outcome of the sensitivity analysis. Column "Mean" gives the average deviation. Columns "Min" and "Max" give the range of deviations. Column "Pop." gives the number of events used to compute the statistics. The event of 31 December 2007 (referenced as "All" in the comments column of Table 1) and the event of 12 June 2008 are excluded. Deviation of γ above $\pm 50^\circ$ are excluded. Positive and negative deviations are entered for the parameters presenting an important skewness. Events when α was degenerate or null are excluded.

Parameter	Min	Mean	Max	Pop.
	(Degrees)			
ϕ	1.5	4.3	16.6	26
θ	0.9	1.8	3.7	26
γ	9	22	48	11
h_{front}	0.20	0.48	1.00	26
κ	+0.02	+0.07	+0.21	26
	−0.02	−0.04	−0.08	
α	+4	+13	+33	18
	−3	−7	−20	

chose to fit the front with a simple hemispherical shell: α is set to 0 and the tilt angle has no effect because of the symmetry of revolution.

To give an estimate of the precision of the different model parameters we performed a sensitivity analysis. This consists of varying one parameter at a time, up until the merit function has decreased by a fixed percentage. In Figure 3, the full width at half maximum (FWHM) and the full width for a 10% decrease of the functions ($\text{FW}_{0.9}$) are also shown on the graphs. We chose to perform the sensitivity analysis with a 10% decrease for two reasons. The first is simply the processing speed: The range of the parameter scan is smaller than for a FWHM, which makes the analysis faster. The second is that, for some parameters such as the tilt angle γ for example, the merit function is π periodic and does not decrease by less than 20% in some cases, so a sensitivity analysis would not be possible with a threshold lower than 20%. Note that the method we use only allows comparing the precision between the parameters of this model and this technique: Comparing those results with the precision given by other techniques might be hazardous if they have not been estimated with this method. Finally, one limitation of this analysis is that we explore the parameter space only one parameter at a time. A more rigorous way would be to use a Monte Carlo method to randomly explore the parameter space around the absolute maximum. It might be interesting to apply this more elaborate and processing-intensive technique in future studies to see how the results differ from the simple sensitivity analysis we used.

Table 2 gives the results of this analysis. We remark that the deviation for the parameters γ and α are an order of magnitude larger than the deviation for the longitude and latitude. This shows that measuring the orientation and the length of a flux rope with this technique is uncertain and difficult. *In situ* measurements as well as investigating the CME propagation from its initiation to 1 AU would probably help to narrow down the estimate. Also, imaging instruments placed away from the ecliptic plane would also certainly help resolve this kind of ambiguity. Finally, we know that the precision of the triangulation method is maximum when the separation between the two views is 90° but we have not been able to observe any decrease of the precision during the studied period, where the separation angle varied from 40° to 65°.

Figure 7 is a polar view summarizing the direction of the 26 events with respect to Earth at the time they were observed. We see that we measured CMEs in almost every longitudinal

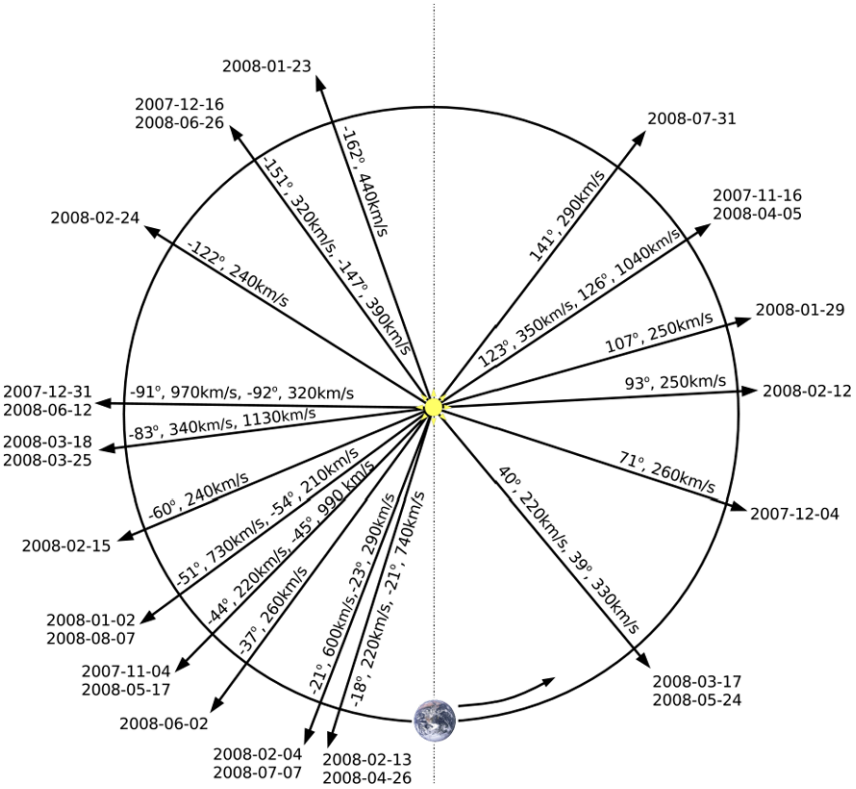

Figure 7 Polar view summarizing the CME directions with respect to Earth when they where observed.

direction, even though the distribution seems to be slightly skewed toward the east: We believe this is more than likely because the population of events is insufficient.

To validate the estimated directions, we compared results with independent measurements and techniques. Colaninno and Vourlidas (2009) have developed a technique to estimate the CME center-of-mass direction by requiring that the same mass should be observed by both COR2 telescopes. A comparison of their results for eight events to our method shows that they are the same to within $\pm 10°$, except for halo CMEs (in one of the telescopes), which reduces the accuracy to $\sim 30°$. The latter discrepancy is due to the larger uncertainty of mass measurements for halo events as discussed in their paper. Another way to test our propagation results is to identify events in our list that are directed toward one of the two STEREO spacecraft and then check for *in situ* signatures for them. This comparison is not as accurate as the one just discussed, since a CME greatly expands by the time it encounters the STEREO spacecraft, which can cross the structure at any point. However, it provides a quick verification of our fitting. A quick comparison with a list of interplanetary coronal mass ejections (ICMEs) investigated by the IMPACT team (Li *et al.*, 2009) reveals four matches. The events on 4 February, 26 April, 2 June, and 7 August, 2008 have been detected by IMPACT-B as we were expecting based on our results (Figure 7). As an example, STEREO-B was located 25° from Earth on 6 June when IMPACT passed close to the central axis of the flux rope within the 2 June 2008 CME. This is only a 12° difference from our estimate of 37° for the longitude of this event. This is only a rough estimate pending further

Table 3 Velocity and acceleration of the 26 events. ϕ is the Stonyhurst longitude from Table 1, V is the 3D velocity of the apex of the model, V_{CDAW} is the projected velocity given by the CDAW catalog, V_p is the projected speed, and a is the 3D acceleration calculated using a second-order fit.

Date	ϕ (degrees)	V	V_{CDAW} (km s^{-1})	V_p	a (m s^{-2})
04-Nov-2007	−44	216	179	150	9.0
16-Nov-2007	123	345	326	289	11.8
04-Dec-2007	71	265	210	251	7.0
16-Dec-2007	−144	325	184	191	4.8
31-Dec-2007	−80	972	1013	957	−5.0
31-Dec-2007 up	−91	846	1013	845	−16.0
31-Dec-2007 low	−91	967	1013	967	−57.0
02-Jan-2008	−51	731	676	568	−6.3
23-Jan-2008	−160	442	362	151	10.4
29-Jan-2008	107	246	166	235	5.0
04-Feb-2008	−21	598	306	214	7.0
12-Feb-2008	93	249	266	249	12.1
13-Feb-2008	−18	225	157	70	2.9
15-Feb-2008	−73	230	163	220	8.2
24-Feb-2008	−122	244	246	207	8.8
17-Mar-2008	40	221	211	142	6.9
18-Mar-2008	−83	340	–	337	8.5
25-Mar-2008	−83	1127	980	1119	−30.6
05-Apr-2008	126	1043	962	843	4.0
26-Apr-2008	−21	741	515	266	1.4
17-May-2008	−45	986	630	697	13.1
24-May-2008	39	331	225	208	6.1
02-Jun-2008	−37	265	–	159	5.0
12-Jun-2008	−102	319	274	312	5.2
26-Jun-2008	−147	389	204	212	0.9
07-Jul-2008	−23	292	–	114	15.0
31-Jul-2008	141	288	–	181	1.8
07-Aug-2008	−54	215	–	174	0.6

analysis of the ICME but it does provide confidence in our technique. We will continue to check our results against other independent estimates as they become available.

We also compared the position on the solar surface of the source regions (SRs) associated with the front-side CMEs. We only found 5 out of 13 front-side CMEs for which it was possible to identify with no ambiguity the associated SR in EUVI (2 January 2008, 4 February 2008, 25 March 2008, 26 April 2008, and 17 May 2008). We found that the directions of these events were always within $\pm 20^{\circ}$ of their associated SR, which is a good agreement since CMEs can be generally slightly deflected compared to their SR, as we found in Thernisien, Howard, and Vourlidas (2006).

Table 3 gives the 3D speed of the model apex, V, and its acceleration, a, for the 26 events. The speeds are calculated by using a first-order fit, and the accelerations with a second-order fit. They are compared to the projected speeds given by the CDAW catalog (Yashiro *et al.*,

2004). We see that V and V_{CDAW} are well correlated and that $V > V_{\mathrm{CDAW}}$ in the large majority of the cases, which makes sense since CDAW provides projected speeds. We calculated in the column V_p the projected speed of the apex, taking into account the direction of the front with respect to Earth, using the formula $V_p = V \sin\phi$. This is an oversimplification of what the rigorous formula should be since it does not take into account the spatial extension of the model: The projected height of the model apex is always lower than or equal to the maximum projected height of the model outer front. Indeed, we see that V_p is lower than V_{CDAW} in most of the cases.

9. Summary

In this paper, we presented a technique that permits us to estimate the 3D direction, speed, and spatial extent of coronal mass ejections. The technique uses a geometric model of a flux rope that is interactively, then automatically, fit to a synchronized pair of STEREO/SECCHI COR2 images. The different points discussed in this paper, as well as the main results, are summarized here:

- A graphic user interface has been implemented and is available in SolarSoft. The fitting method has been described in detail so that the reader can reproduce the results and use the technique for other events not treated here.
- The technique is fast; only few minutes are necessary for a trained user to perform a fitting.
- A merit function was used to partially automate the fit and to perform a sensitivity analysis. This allowed us to calculate a maximum precision of $\pm 17^\circ$ for the longitude and $\pm 4^\circ$ for the latitude, for a decrease of 10% of the merit function.
- It was not possible to determine in all the cases the flux-rope orientation and/or its length. The sensitivity analysis revealed that the precision of those two parameters is large compared to the precision of the longitude and latitude. A deeper investigation of the CME source region magnetic field and the CME propagation from the low corona through the fields of views of the SECCHI and SOHO imaging instruments, as well *in situ* signature measurements at 1 AU, would certainly be necessary to determine these parameters.
- The CME direction determined with the independent technique of Colaninno and Vourlidas (2009) has shown good agreement with our results for eight events.
- Comparison with *in situ* signatures of CMEs at 1 AU also show good agreement for four events. Further comparison with other reconstruction methods would certainly be useful to cross-validate the different methods.
- Comparison between the CME SR position and the CME direction for the front-side events show that they were within $\pm 20^\circ$, but we could identify with no ambiguity only 5 out of 13 front-side CMEs with an associated SR on the disk. This point should be investigated in a future study.
- Comparison of 3D speed and projected speed from the CDAW catalog show a good correlation, but direct correction of the projection effects cannot be done without taking into account the spatial extent of the CME.

For future studies, we plan to implement an extra parameter to "morph" the model so it can better fit events with a distorted front. A hybrid reconstruction of such CMEs, using both forward modeling and tomography, could also be used, as shown by Antunes, Thernisien, and Yahil (2009). Finally, Ontiveros and Vourlidas (2009) used a similar forward modeling technique to study shocks associated with CMEs observed in LASCO images. We can

imagine combining their shock model with our GCS model and taking advantage of the two viewpoints provided by STEREO to study the properties of these two structures.

Acknowledgements The STEREO/SECCHI data used here are produced by an international consortium of the Naval Research Laboratory (USA), Lockheed Martin Solar and Astrophysics Lab (USA), NASA Goddard Space Flight Center (USA), Rutherford Appleton Laboratory (UK), University of Birmingham (UK), Max-Planck-Institut für Sonnensystemforschung (Germany), Centre Spatiale de Liège (Belgium), Institut d'Optique Théorique et Appliquée (France), and Institut d'Astrophysique Spatiale (France). The NRL effort was supported by NASA, the USAF Space Test Program, and the Office of Naval Research.

References

Antunes, A., Thernisien, A., Yahil, A.: 2009, Hybrid reconstruction to derive 3D height-time evolution for Coronal Mass Ejections. *Solar Phys.* submitted.

Billings, D.E.: 1966, *A Guide to the Solar Corona*, Academic Press, New York.

Boursier, Y.: 2007, Ejections coronales de masse: détection, propriétés statistiques et reconstruction 3D. PhD thesis, Université Paul Cézanne – Aix-Marseille III.

Boursier, Y., Lamy, P., Llebaria, A.: 2009, Three-dimensional kinematics of coronal mass ejections from STEREO/SECCHI-COR2 observations in 2007 – 2008. *Solar Phys.* this issue.

Brueckner, G.E., Howard, R.A., Koomen, M.J., Korendyke, C.M., Michels, D.J., Moses, J.D., Socker, D.G., Dere, K.P., Lamy, P.L., Llebaria, A., Bout, M.V., Schwenn, R., Simnett, G.M., Bedford, D.K., Eyles, C.J.: 1995, The Large Angle Spectroscopic Coronagraph (LASCO). *Solar Phys.* **162**, 357 – 402.

Calabretta, M.R., Greisen, E.W.: 2002, Representations of celestial coordinates in FITS. *Astron. Astrophys.* **395**, 1077 – 1122. doi:10.1051/0004-6361:20021327.

Chen, J.: 1996, Theory of prominence eruption and propagation: interplanetary consequences. *J. Geophys. Res.* **101**, 27499 – 27520. doi:10.1029/96JA02644.

Chen, J., Howard, R.A., Brueckner, G.E., Santoro, R., Krall, J., Paswaters, S.E., St. Cyr, O.C., Schwenn, R., Lamy, P., Simnett, G.M.: 1997, Evidence of an erupting magnetic flux rope: LASCO coronal mass ejection of 13 April 1997. *Astrophys. J.* **490**, L191. doi:10.1086/311029.

Chen, J., Santoro, R.A., Krall, J., Howard, R.A., Duffin, R., Moses, J.D., Brueckner, G.E., Darnell, J.A., Burkepile, J.T.: 2000, Magnetic geometry and dynamics of the fast coronal mass ejection of 9 September 1997. *Astrophys. J.* **533**, 481 – 500.

Colaninno, R.C., Vourlidas, A.: 2009, First determination of the true mass of coronal mass ejections: a novel approach to using the two STEREO viewpoints. arXiv:0903.4344.

Cremades, H., Bothmer, V.: 2004, On the three-dimensional configuration of coronal mass ejections. *Astron. Astrophys.* **422**, 307 – 322.

Eyles, C.J., Simnett, G.M., Cooke, M.P., Jackson, B.V., Buffington, A., Hick, P.P., Waltham, N.R., King, J.M., Anderson, P.A., Holladay, P.E.: 2003, The solar mass ejection imager (SMEI). *Solar Phys.* **217**, 319 – 347.

Fisher, R.R., Munro, R.H.: 1984, Coronal transient geometry. I – The flare-associated event of 25 March 1981. *Astrophys. J.* **280**, 428 – 439. doi:10.1086/162009.

Forbes, T.G., Linker, J.A., Chen, J., Cid, C., Kóta, J., Lee, M.A., Mann, G., Mikić, Z., Potgieter, M.S., Schmidt, J.M., Siscoe, G.L., Vainio, R., Antiochos, S.K., Riley, P.: 2006, CME theory and models. *Space Sci. Rev.* **123**, 251 – 302. doi:10.1007/s11214-006-9019-8.

Frazin, R.A., Janzen, P.: 2002, Tomography of the solar corona. II. Robust, regularized, positive estimation of the three-dimensional electron density distribution from LASCO-C2 polarized white-light images. *Astrophys. J.* **570**, 408 – 422. doi:10.1086/339572.

Frazin, R.A., Kamalabadi, F.: 2005a, On the use of total brightness measurements for tomography of the solar corona. *Astrophys. J.* **628**, 1061 – 1069. doi:10.1086/430846.

Frazin, R.A., Kamalabadi, F.: 2005b, Rotational tomography for 3D reconstruction of the white-light and EUV corona in the post-SOHO era. *Solar Phys.* **228**, 219 – 237. doi:10.1007/s11207-005-2764-0.

Frazin, R.A., Butala, M.D., Kemball, A., Kamalabadi, F.: 2005, Time-dependent reconstruction of nonstationary objects with tomographic or interferometric measurements. *Astrophys. J.* **635**, L197 – L200. doi:10.1086/499431.

Howard, R.A., Sheeley, N.R. Jr., Michels, D.J., Koomen, M.J.: 1985, Coronal mass ejections – 1979 – 1981. *J. Geophys. Res.* **90**, 8173 – 8191.

Howard, R.A., Moses, J.D., Vourlidas, A., Newmark, J.S., Socker, D.G., Plunkett, S.P., Korendyke, C.M., Cook, J.W., Hurley, A., Davila, J.M., Thompson, W.T., St Cyr, O.C., Mentzell, E., Mehalick, K., Lemen,

J.R., Wuelser, J.P., Duncan, D.W., Tarbell, T.D., Wolfson, C.J., Moore, A., Harrison, R.A., Waltham, N.R., Lang, J., Davis, C.J., Eyles, C.J., Mapson-Menard, H., Simnett, G.M., Halain, J.P., Defise, J.M., Mazy, E., Rochus, P., Mercier, R., Ravet, M.F., Delmotte, F., Auchere, F., Delaboudiniere, J.P., Bothmer, V., Deutsch, W., Wang, D., Rich, N., Cooper, S., Stephens, V., Maahs, G., Baugh, R., McMullin, D., Carter, T.: 2008, Sun Earth connection coronal and heliospheric investigation (SECCHI). *Space Sci. Rev.* **136**, 67 – 115. doi:10.1007/s11214-008-9341-4.

Illing, R.M.E., Hundhausen, A.J.: 1985, Observation of a coronal transient from 1.2 to 6 solar radii. *J. Geophys. Res.* **90**, 275 – 282.

Jackson, B.V., Buffington, A., Hick, P.P., Wang, X., Webb, D.: 2006, Preliminary three-dimensional analysis of the heliospheric response to the 28 October 2003 CME using SMEI white-light observations. *J. Geophys. Res.* **111**, 4. doi:10.1029/2004JA010942.

Krall, J., St. Cyr, O.C.: 2006, Flux-rope coronal mass ejection geometry and its relation to observed morphology. *Astrophys. J.* **652**, 1740 – 1746. doi:10.1086/508337.

Li, Y., Kilpua, E., Lynch, B., Luhmann, J., Toy, A., Vourlidas, A., Jian, L., Russell, C., Galvin, A., Acuna, M., Sauvaud, J.A., Skoug, R., Schroeder, P., Petrie, G.: 2009, Personal Communication.

Liewer, P.C., Dejong, E.M., Hall, J.R., Braswell, S.J., Thompson, W.T., Howard, R.: 2007, Stereoscopic analysis of CME-related coronal activity using STEREO/SECCHI observations. *AGU Fall Meeting Abstracts*, 2.

Liewer, P.C., Dejong, E.M., Hall, J.R., Huttunen, K.J., Howard, R.A., Vourlidas, A., Thompson, W.T.: 2008, Stereoscopic analysis of STEREO/EUVI observations of 19 May 2007 erupting filament. *AGU Spring Meeting Abstracts*, 4.

Liewer, P.C., De Jong, E.M., Hall, J.R., Howard, R.A., Thompson, W.T., Culhane, J.L., Bone, L.A., Van Driel-Gesztelyi, L., 2009, Stereoscopic analysis of the 19 May 2007 erupting filament. *Solar Phys.* this issue.

Mierla, M., Davila, J., Thompson, W., Inhester, B., Srivastava, N., Kramar, M., St. Cyr, O.C., Stenborg, G., Howard, R.A.: 2008, A quick method for estimating the propagation direction of coronal mass ejections using STEREO-COR1 images. *Solar Phys.* **252**, 385 – 396. doi:10.1007/s11207-008-9267-8.

Minnaert, M.: 1930, On the continuous spectrum of the corona and its polarisation. With 3 figures. (Received 30 July 1930). *Z. Astrophys.* **1**, 209.

Ontiveros, V., Vourlidas, A.: 2009, Quantitative measurements of coronal mass ejection-driven shocks from LASCO observations. *Astrophys. J.* **693**, 267 – 275. doi:10.1088/0004-637X/693/1/267.

Pizzo, V.J., Biesecker, D.A.: 2004, Geometric localization of STEREO CMEs. *Geophys. Rev. Lett.* **31**, 21802. doi:10.1029/2004GL021141.

Press, W.H., Teukolsky, S.A., Vetterling, W.T., Flannery, B.P.: 2003, *Numerical Recipes*, 2nd edn. Cambridge University Press, Cambridge.

Puetter, R.C., Gosnell, T.R., Yahil, A.: 2005, Digital image reconstruction: deblurring and denoising. *Annu. Rev. Astron. Astrophys.* **43**, 139 – 194.

Quémerais, E., Lamy, P.: 2002, Two-dimensional electron density in the solar corona from inversion of white light images – application to SOHO/LASCO-C2 observations. *Astron. Astrophys.* **393**, 295 – 304.

Saito, K., Poland, A.I., Munro, R.H.: 1977, A study of the background corona near solar minimum. *Solar Phys.* **55**, 121 – 134.

Thernisien, A.F.R., Howard, R.A., Vourlidas, A.: 2006, Modeling of flux rope coronal mass ejections. *Astrophys. J.* **652**, 763 – 773. doi:10.1086/508254.

Thompson, W.T.: 2006, Coordinate systems for solar image data. *Astron. Astrophys.* **449**, 791 – 803. doi:10.1051/0004-6361:20054262.

Van de Hulst, H.C.: 1950, The electron density of the solar corona. *Bull. Astron. Inst. Neth.* **11**, 135.

Vásquez, A.M., Frazin, R.A., Hayashi, K., Sokolov, I.V., Cohen, O., Manchester, W.B. IV, Kamalabadi, F.: 2008, Validation of two MHD models of the solar corona with rotational tomography. *Astrophys. J.* **682**, 1328 – 1337. doi:10.1086/589682.

Vourlidas, A., Subramanian, P., Dere, K.P., Howard, R.A.: 2000, Large-angle spectrometric coronagraph measurements of the energetics of coronal mass ejections. *Astrophys. J.* **534**, 456 – 467. doi:10.1086/308747.

Xie, H., Ofman, L., Lawrence, G.: 2004, Cone model for halo CMEs: application to space weather forecasting. *J. Geophys. Res.* **109**, 3109. doi:10.1029/2003JA010226.

Yashiro, S., Gopalswamy, N., Michalek, G., St. Cyr, O.C., Plunkett, S.P., Rich, N.B., Howard, R.A.: 2004, A catalog of white light coronal mass ejections observed by the SOHO spacecraft. *J. Geophys. Res.* **109**, 7105. doi:10.1029/2003JA010282.

Zhao, X.P.: 2008, Inversion solutions of the elliptic cone model for disk frontside full halo coronal mass ejections. *J. Geophys. Res.* **113**, 2101. doi:10.1029/2007JA012582.

Zhao, X.P., Plunkett, S.P., Liu, W.: 2002, Determination of geometrical and kinematical properties of halo coronal mass ejections using the cone model. *J. Geophys. Res.* **107**, 1223. doi:10.1029/2001JA009143.